

Revision 1

Synthesis and crystal structure of Mg-bearing Fe₉O₁₁: New insight in the complexity of Fe-Mg oxides at conditions of the deep upper mantle

Takayuki Ishii^{1,*}, Laura Uenver-Thiele², Alan B. Woodland², Edith Alig³, Tiziana Boffa

Ballaran¹

¹*Bayerisches Geoinstitut, Universität Bayreuth, D - 95440 Bayreuth, Germany*

²*Institut für Geowissenschaften, Goethe-Universität Frankfurt, Altenhöferallee 1, D – 60438*

Frankfurt am Main, Germany

³*Institut für Anorganische und Analytische Chemie, Goethe-Universität Frankfurt,*

Max-von-Laue-Str. 7, D-60438 Frankfurt am Main, Germany

ABSTRACT

A novel Mg-bearing iron oxide Mg_{0.87(1)}Fe²⁺_{4.13(1)}Fe³⁺₄O₁₁ was synthesized at 12 GPa and 1300 °C using a large volume press. Rietveld structural analysis was conducted with a laboratory X-ray diffraction pattern obtained at ambient conditions. The crystal structure, which has one oxygen trigonal prism site and four octahedral sites for the cations, was found to be

isostructural with $\text{Ca}_2\text{Fe}_7\text{O}_{11}$. The unit-cell lattice parameters are $a = 9.8441(5) \text{ \AA}$, $b = 2.8920(1) \text{ \AA}$, $c = 14.1760(6) \text{ \AA}$, $\beta = 99.956(4)^\circ$, $V = 397.50(3) \text{ \AA}^3$, and $Z = 2$ (monoclinic, $C2/m$). Mg and Fe cations are disordered on the trigonal prism site and on two of the four octahedral sites, and the remaining Fe is accommodated at the other two octahedral sites. The present structure is closely related to the other recently discovered Fe oxide structures, e.g. Fe_4O_5 and Fe_5O_6 , by distortion derived either from incorporation (Fe_4O_5) or removal (Fe_5O_6) of an edge-shared FeO_6 single octahedral chain in their structures. The present synthesis at deep upper mantle conditions and the structural relationships observed between various novel Mg-Fe oxides indicate that a series of different phases become stable above 10 GPa and that their relative stabilities ($\text{Fe}^{2+}/\text{Fe}^{3+}$) must be controlled by oxygen fugacity.

Keywords: Iron oxide, High-pressure synthesis, Walker-type multi-anvil apparatus, Rietveld analysis, X-ray diffraction, Fe_9O_{11}

INTRODUCTION

The Fe-O system is fundamental for understanding redox processes operating in the Earth's interior. The iron oxides, Fe^{2+}O wüstite, $\text{Fe}^{2+}\text{Fe}^{3+}_2\text{O}_4$ magnetite and $\text{Fe}^{3+}_2\text{O}_3$ hematite, have been known for a long time and their relative stabilities are directly related to the local

oxygen fugacity (fO_2) that controls the Fe^{3+}/Fe^{2+} in mineral assemblages. Recent experimental studies have revealed several new mixed-valence Fe-oxides to be stable at high pressures and temperatures, such as the orthorhombic-structured phases $Fe^{2+}_2Fe^{3+}_2O_5$ and $Fe^{2+}_3Fe^{3+}_2O_6$ (Lavina et al. 2011; Woodland et al. 2012; Woodland et al. 2015; Lavina and Meng, 2015). More recently, Sinmyo et al. (2016) reported the synthesis of monoclinic-structured $Fe^{2+}_3Fe^{3+}_4O_9$ at 25 GPa. These discoveries imply that a number of iron oxides with different stoichiometries may be stable at conditions corresponding to the deep upper mantle and transition zone.

These three new high-pressure Fe-oxides are structurally related to calcium titanite (CT)-type Fe_3O_4 , which is a high-pressure polymorph of magnetite (Haavik et al. 2000; Dubrovinsky et al. 2003). They also follow similar structural systematics to those observed in the family of Ca-ferrite-based phases (Evrard et al. 1980). CT-type Fe_3O_4 consists of double chains of edge-shared FeO_6 octahedra running parallel to one of the orthorhombic cell axes. Corner- and edge-sharing of the four double chains forms an octahedral framework with a tunnel-like space, in which Fe coordination is trigonal prismatic. The stoichiometry of the new iron oxides can be expressed as $Fe^{2+}_{1+n}Fe^{3+}_2O_{4+n}$ (where $n = 0$ for Fe_3O_4 , $n = 0.5$ for Fe_7O_9 , $n = 1$ for Fe_4O_5 and $n = 2$ for Fe_5O_6) by addition of FeO_6 octahedral blocks into a CT-type Fe_3O_4 structure (Evrard et al., 1980; Guignard and Crichton, 2014; Sinmyo et al. 2016; Bykova et al. 2016). Thus, additional

high-pressure iron oxides with other values of n are expected to be stable. It has been also demonstrated that Fe_4O_5 and Fe_7O_9 form solid solutions with the Mg-endmembers such as $\text{Mg}_2\text{Fe}_2\text{O}_5$ and $\text{Mg}_3\text{Fe}_4\text{O}_9$, suggesting possible existence of complicated Mg-Fe oxides in the deep mantle (Boffa Ballaran et al. 2015; Uenver-Thiele et al. 2017a, 2017b).

Recently, a new monoclinic $\text{Fe}^{2+}_5\text{Fe}^{3+}_4\text{O}_{11}$ phase corresponding to $\text{Fe}^{2+}_{1+n}\text{Fe}^{3+}_2\text{O}_{4+n}$ [$n = 1.5$] was reported by Woodland et al. (2016) from a synthesis experiment at 11 GPa. Although the powder diffraction pattern was consistent with a $\text{Ca}_2\text{Fe}_7\text{O}_{11}$ -type structure (Malaman et al. 1981), it could not be analyzed in detail because of extensive peak overlap with coexisting phases and the crystal quality precluded analysis by single-crystal diffraction. In this study, we successfully synthesized a single phase of Fe_9O_{11} phase by doping a small amount of Mg component, namely $\text{Mg}_{0.9}\text{Fe}_{8.1}\text{O}_{11}$. We report the synthesis and crystal structure of $\text{Mg}_{0.9}\text{Fe}_{8.1}\text{O}_{11}$ analyzed by the Rietveld method. We also discuss its structural relationship to the family of Mg-Fe oxides and its potential stability in the mantle.

EXPERIMENTAL METHODS

High-pressure high-temperature synthesis

The starting material was a stoichiometric mixture of pre-synthesized $\text{MgFe}^{3+}_2\text{O}_4$

[magnesioferrite (Mf)], $\text{Fe}^{2+}\text{Fe}^{3+}_2\text{O}_4$ [magnetite (Mt)] and Fe^0 metal powder (Chempur, 99.5%) with a grain size $\leq 10 \mu\text{m}$, giving a nominal composition of $\text{Mg}_{0.5}\text{Fe}^{2+}_{2.5}\text{Fe}^{3+}_2\text{O}_6$. Details of the syntheses and characterizations of Mf and Mt are described in Uenver-Thiele et al. (2017a) and Schollenbruch et al. (2011), respectively. The unit-cell parameters for Mf and Mt are $a_o = 8.3875(1) \text{ \AA}$ and $a_o = 8.3966(6) \text{ \AA}$, respectively. The starting materials were ground together under acetone and dried in an oven at $130 \text{ }^\circ\text{C}$.

The synthesis experiment (run no. M702) was performed at 12 GPa and $1300 \text{ }^\circ\text{C}$ using an 800 t Walker-type multi-anvil press (Walker et al. 1990) at the University of Frankfurt using the experimental setup and pressure calibration described by Brey et al. (2008). We used tungsten carbide second-stage anvils with a truncated edge length of 8 mm. The pressure assembly comprised a Cr_2O_3 -doped MgO octahedron (14-mm edge length) with a Re-foil as heater. The starting mixture was packed into a Pt-foil capsule and sealed by hammering. The temperature was monitored using a $\text{W}_3\text{Re}_{97}\text{-W}_{25}\text{Re}_{75}$ thermocouple with the electromotive force uncorrected for pressure. Uncertainties in pressure and temperature are 0.3 GPa and $50 \text{ }^\circ\text{C}$, respectively (Brey et al. 2008). The assembly was first pressurized at room temperature and subsequently heated ($\sim 50 \text{ }^\circ\text{C}/\text{min}$) to the target temperature. After the temperature was kept for 4 h, the sample was quenched (\sim cooling rate of $200\text{-}250 \text{ }^\circ\text{C}/\text{s}$) by turning off the electrical power to the heater,

followed by decompression.

Sample analyses and Rietveld structure refinements

The recovered sample consisted of loose shiny black grains (up to 200 μm) with an irregular form rather than a compact sintered aggregate so that the original texture could not be discerned. A number of these grains were embedded in epoxy, polished and carbon-coated for element analysis (Mg, Fe and Pt) with JEOL JXA-8900 Superprobe at the University of Frankfurt operated at 15 kV and 20 nA. Compositional data were collected using a 1- μm diameter spot size in wavelength-dispersive mode with integration times of 40 s on the background and 20 s on the peak for Fe and Pt. For Mg, counting times on both background and peak were 40 s.

The sample was also investigated with a Renishaw micro-Raman spectrometer (RM-1000) equipped with a 633 nm HeNe laser at the University of Frankfurt. The spectrometer was calibrated using the 519 cm^{-1} peak of a Si wafer (Temple and Hathaway, 1973). Unpolarized confocal Raman spectra were collected with laser power of ~ 10 mW and a 50x microscope objective that gave a spot size of ~ 2 μm in diameter. Wavenumber accuracy is approximately ± 2 cm^{-1} .

Powder X-ray diffraction (XRD) measurement of the recovered sample was conducted

using a STOE Stadi P diffractometer equipped with a Mythen detector at the University of Frankfurt. XRD patterns were collected at ambient conditions in transmission mode between 1° – 100° 2θ , using monochromatic Mo $K\alpha_1$ ($\lambda = 0.70926 \text{ \AA}$) radiation operated at 45 kV and 35 mA. The sample material was mounted in a capillary together with a small amount of silicon as an internal standard. The GSAS software package (Larson and van Dreele, 2000) with the EXPGUI interface (Toby, 2001) was employed for phase identification and determination of unit-cell parameters of the sample.

The powder X-ray diffraction pattern of the recovered sample was analyzed by the Rietveld method using the RIETAN-FP/VENUS package (Izumi and Momma, 2007). Crystal structures were drawn using the VESTA software (Momma and Izumi, 2011). The atomic positions of $\text{Ca}_2\text{Fe}_7\text{O}_{11}$ (Malaman et al. 1981) were adopted as the initial structure model, along with lattice parameters determined from our sample. We converted their structure model to a standard setting for a monoclinic unit cell by using a transformation matrix of \mathbf{a} , \mathbf{b} , $-\mathbf{a}-\mathbf{c}$. The 2θ range between 12.5° – 13° was not considered because of the large asymmetry of the 111 reflection of Si which was difficult to model. A Legendre polynomial function with 12 parameters was used for fitting the background. Initially, the site distributions of Mg and Fe cations were refined on all structural sites constraining the total amount of Mg and Fe to be equal

to the chemical composition obtained from the EMPA within uncertainties; however Mg occupancies at the M4 and M5 sites resulted in negative values. Therefore, we considered Mg only at the M1, M2 and M3 sites. All atoms were refined isotropically, however in order to avoid large correlations between occupancy factors and displacement parameters (U_{iso}), we have introduced the following constraints: the less distorted octahedral sites M2 and M3 were constrained to have the same U_{iso} , a similar constraint was applied to the two more distorted octahedral sites M4 and M5 and to the oxygen atoms. In the final stage of the analysis, lattice parameters, a scale factor, atomic coordinates, site occupancies, isotropic atomic displacement parameters, and a split-type pseudo-Voigt profile fitting function (Toraya, 1990) were refined simultaneously. Silicon mixed with the sample was included in the Rietveld analysis as an extra phase, with its scale factor and isotropic atomic displacement parameter also refined. The results of the Rietveld analysis are summarized in Figure 1 and Table 1.

RESULTS AND DISCUSSION

The recovered sample has a composition of 91.2(5) wt% FeO and 5.46(4) wt% MgO (average of 18 spot measurements). Given that the X-ray powder diffraction pattern is consistent with an ideal $M^{2+}_5M^{3+}_4O_{11}$ phase, we have recalculated the FeO content in terms of Fe^{2+} and Fe^{3+}

according to this stoichiometry resulting in the following composition: $\text{Mg}_{0.87(1)}\text{Fe}_{4.13(1)}^{2+}\text{Fe}_{4}^{3+}\text{O}_{11}$.

No further phases were identified. The recovered phase has a slightly higher Fe^{3+} content than the starting material. This may be related to minor Fe-loss to the Pt capsule, which leads to a slight excess of oxygen in the sample and subsequent oxidation. This effect was clearly of limited extent since the difference in Fe content between the starting material and the recovered sample is only $\sim 2\%$.

To check the possibility of inadvertent H incorporation into this phase during the experiment (i.e. although no H_2O was added, H is known to be mobile during high-pressure experiments), Raman spectra were obtained on a number of crystals. No peaks were observed in the range of $2500 - 4000 \text{ cm}^{-1}$, indicating that no appreciable H is present.

The derived crystal structure of $\text{Mg}_{0.9}\text{Fe}_{8.1}\text{O}_{11}$ is presented in Figure 2. The crystal structure of $\text{Mg}_{0.9}\text{Fe}_{8.1}\text{O}_{11}$ has five non-equivalent (M1, M2, M3, M4, M5) sites for cations, in which the M1 site is a trigonal prism and the others are octahedrally coordinated sites (Fig. 2). Mg appears to preferentially occupy the M3 site and it is present only in minor amounts at the M1 and M2 sites, whereas M4 and M5 accommodate only Fe. The displacement parameter of the M4 and M5 sites is slightly larger than that of the other polyhedral sites, likely due to the fact that an isotropic displacement cannot model the motions of Fe occupying these positions. It should be

noted that the coordination of the M4 and M5 sites is closer to a square pyramid than to an octahedron given that the M4-O1 and the M5-O6 bond distances are significantly longer than any other M4-O and M5-O distances (Table 1). This may be the cause of some dynamic disorder at these sites, resulting in larger U_{iso} . The U_{iso} of the oxygen atoms is slightly smaller than those obtained for the cation sites. This is likely due to the fact that oxygen is a light scattering element and, therefore, it is more difficult to accurately constrain its motion from powder diffraction data. However, fixing the oxygen U_{iso} to a value similar to those of the cation sites (i.e. $U_{iso} = 0.01$) results in identical Mg/Fe site occupancies. The four octahedral sites form a framework of corner- and edge-sharing polyhedra around tunnel-shaped spaces running parallel to the b -axis in which the trigonal prisms are situated (Fig. 2). It is not possible to distinguish between Fe^{2+} and Fe^{3+} in a structural refinement; therefore in our model we simply refined Mg vs Fe occupancies. It is possible, however, to obtain some indication whether a site is prevalently occupied by Fe^{2+} or Fe^{3+} by analyzing polyhedral bond distances and volumes. The average M1-O distance of the M1O₆ trigonal prism site is 2.206 Å (Table 1), which is only slightly larger to that calculated using the effective ionic radii of Mg²⁺, Fe²⁺ and O²⁻ in six-fold coordination ($r_{Mg} = 0.72$ Å, $r_{Fe^{2+}} = 0.780$ Å and $r_O = 1.40$ Å, respectively) and Mg-Fe site distribution, 2.177 Å ($r_{Fe^{2+}} \times 0.94 + r_{Mg} \times 0.06 + r_O$) (Shannon, 1976). In addition, the bond valence sum (BVS) (Brown and Altermatt,

1985) for the M1 cation, which was calculated from the M1 cation-oxygen bond lengths, is +1.71 suggesting that ferric iron does not occupy this site. The average cation-oxygen distances of the M2O₆ and M3O₆ sites are 1.992 and 2.097 Å, respectively, which are relatively short compared with values calculated from the ion radii in the same way as for the M1 site (2.175 and 2.160 Å, respectively), suggesting that part of the Fe present in this sites is Fe³⁺. The average cation-oxygen distances of the M4O₆ and M5O₆ sites are 2.055 and 2.127 Å, respectively. These are relatively long compared with the theoretical value of 2.045 Å considering only Fe³⁺ (0.645 Å) and O²⁻ in six-fold coordination. However, both octahedra are very distorted, with one of the six bond lengths much longer than the other five. Considering that square pyramid coordination for these two sites considerably reduces their polyhedral volumes (Table 1), this may explain why no Mg is partitioned onto these cation sites. The effective coordination numbers, n_c , (Hoppe, 1979) for M4 (5.00) and M5 (4.75) further support the assumption of a 5-fold coordination environment (Table 1). Malaman et al. (1981) reported a similar geometry for Ca₂Fe₇O₁₁. Note that the n_c for M2 (5.90) and M3 (5.77) (Table 1), are consistent with octahedral coordination. The BVS of M3, +2.19, is in excellent agreement with the presence of most of the Mg cations at this site; whereas the other BSV all smaller than +3 (Table 1) suggest some degree of Fe²⁺-Fe³⁺ disordering, as also has been suggested for Mg₂Fe₂O₅ and Fe₇O₉ (Boffa-Ballaran et al. 2015;

Sinmyo et al. 2016).

Woodland et al. (2016) determined the lattice parameters of Fe_9O_{11} ($a = 9.8841(6) \text{ \AA}$, $b = 2.8842(1) \text{ \AA}$, $c = 14.1919(7) \text{ \AA}$, $\beta = 99.924(6)^\circ$ and $V = 398.52(2) \text{ \AA}^3$, transformed to the standard setting), where a and c are longer and b is slightly shorter, than those obtained for $\text{Mg}_{0.9}\text{Fe}_{8.1}\text{O}_{11}$. The smaller volume of our solid solution ($V = 397.50 \text{ \AA}^3$) is reasonable because of substitution of Fe^{2+} by Mg with smaller ionic radius. The larger b -axis for the solid solution suggests that Fe^{3+} may be incorporated into the trigonal prism site in the Fe_9O_{11} endmember, whereas is likely not present at this site in our sample.

The structure of $\text{Mg}_{0.9}\text{Fe}_{8.1}\text{O}_{11}$ is compared with those of other recently discovered high-pressure iron-oxides in Figure 3, which summarizes changes in crystal structure with $\text{Fe}^{3+}/(\text{Mg}+\Sigma\text{Fe})$ ratio. In a sequence of the orthorhombic structures $X_3\text{O}_4$, $X_4\text{O}_5$ and $X_5\text{O}_6$ ($X = \text{Fe}^{2+}$, Fe^{3+} , Mg) with decreasing $\text{Fe}^{3+}/(\text{Mg}+\Sigma\text{Fe})$ ratio, two single chains of $(\text{Mg},\text{Fe}^{2+})\text{O}_6$ octahedra are added symmetrically to a tunnel-shaped space as discussed by Malaman et al. (1981) and Guignard and Crichton (2014). The change from the orthorhombic to monoclinic structures of $X_7\text{O}_9$ and $X_9\text{O}_{11}$ is explained by incorporating a single $(\text{Mg},\text{Fe}^{2+})\text{O}_6$ octahedral chain into the $X_3\text{O}_4$ and $X_4\text{O}_5$ phases, respectively. This breaks a mirror plane of the tunnel-shaped spaces, resulting in distortion of the orthorhombic unit cell to one that is monoclinic.

IMPLICATIONS

$\text{Mg}_{0.9}\text{Fe}_{8.1}\text{O}_{11}$ is a new high-pressure iron-rich oxide with $\text{Ca}_2\text{Fe}_7\text{O}_{11}$ -type structure, suggesting that the Fe_9O_{11} endmember also may have the same crystal structure. Our synthesis indicates that at least ~20 % of the $\text{Mg}_5\text{Fe}^{3+}_4\text{O}_{11}$ component can be incorporated into Fe_9O_{11} . Although complete Fe^{2+} -Mg solid solution remains to be demonstrated, analogy with the structurally related phases (Mg,Fe^{2+}) $_2\text{Fe}^{3+}_2\text{O}_5$ (Lavina et al. 2011; Boffa Ballaran et al. 2015; Uenver-Thiele et al. 2018) and (Mg,Fe^{2+}) $_3\text{Fe}^{3+}_4\text{O}_9$ (Sinmyo et al. 2016; Uenver-Thiele et al. 2017b) suggests that this may be the case for Fe_9O_{11} as well.

Myhill et al. (2016) calculated that Fe_4O_5 ($\text{Fe}^{3+}/\Sigma\text{Fe} = 0.5$) is stable at oxygen fugacities above those at which diamond is stable, but that the redox stability of Fe_5O_6 ($\text{Fe}^{3+}/\Sigma\text{Fe} = 0.4$) overlaps with that of diamond. Since the $\text{Fe}^{3+}/\Sigma\text{Fe}$ (0.44) of Fe_9O_{11} is intermediate between Fe_4O_5 and Fe_5O_6 , it also may be possible that the redox stability of Fe_9O_{11} is compatible with diamond. This study demonstrates the stability of yet another Fe-Mg oxide phase at conditions corresponding to the deeper portion of the upper mantle and transition zone. Unlike at low pressures where magnetite can coexist over a wide range of $f\text{O}_2$ with either Fe_xO or Fe_2O_3 , at pressures > 8-10 GPa a series of discrete Fe-Mg oxide phases with different stoichiometries become stable depending on the ambient $f\text{O}_2$. The addition of Mg to each of these phases will

change the $\text{Fe}^{3+}/\Sigma\text{Fe}$ and thus have a strong effect on their redox stabilities. This adds an extra complexity when attempting to understand phase relations of “simple” oxides as a function of $f\text{O}_2$.

The recovery of these high-pressure oxides is not always possible because they revert to the spinel structure during decompression or sample preparation. It has been shown that back reaction of Fe_4O_5 (Schollenbruch et al. 2011; Myhill et al, 2016) gives rise to magnetite with a peculiar twinning on {311} planes which appear to be aligned along the planes formed by the trigonal prisms perpendicular to the c -axis of the Fe_4O_5 structure. Uenver-Thiele et al. (2017b) has therefore reinterpreted the observations of Jacob et al. (2016) of a magnetite inclusion in diamond that exhibited twinning on the {311} planes as providing indirect evidence for Fe_4O_5 having grown syngenetically with diamond. Considering the structural similarities between Fe_4O_5 , Fe_5O_6 and Fe_9O_{11} , all presenting planes containing the trigonal prism sites repeat in the c -direction (Fig. 3), it is possible that one of the latter two phases also could have been the precursor, similarly producing twinning on {311} planes in magnetite during an oxidizing transformation reaction.

ACKNOWLEDGMENTS

This project was supported by grants from the Deutsche Forschungsgemeinschaft (DFG)

to ABW (Wo 652/20-2) and TBB (Bo 2550/7-2). T.I. has been supported by an Alexander von Humboldt Postdoctoral Fellowship.

REFERENCES CITED

- Boffa Ballaran, T., Uenver-Thiele, L., Woodland, A.B., and Frost, D.J. (2015) Complete substitution of Fe²⁺ by Mg in Fe₄O₅: The crystal structure of the Mg₂Fe₂O₅ end-member. *American Mineralogist*, 100, 628–632.
- Brey, G.P., Bulatov, V., and Gurnis, A. (2008): Geobarometry for peridotites: experiments in simple and natural systems from 6 to 10 GPa. *Journal of Petrology*, 49, 3–24.
- Brown, I.D., Altermatt, D. (1985) Bond-valence parameters obtained from a systematic analysis of the Inorganic Crystal Structure Database. *Acta Crystallographica*, B41, 244–247.
- Bykova, E., Dubrovinsky, L., Dubrovinskaia, N., Bykov, M., McCammon, C., Ovsyannikov, S. V., Liermann, H. -P., Kuppenko, I., Chumakov, A. I., Rüffer, R., Hanfland, M. and Hanfland, M. (2016) Structural complexity of simple Fe₂O₃ at high pressures and temperatures. *Nature Communications*, 7, 10661.
- Dubrovinsky, L.S., Dubrovinskaia, N.A., McCammon, C., Rozenberg, G.K., Ahuja, R., Osorio-Guillen, M.V., Dmitriev, J., Weber, H.P., Le Bihan, T., and Johansson, B. (2003) The structure of the metallic high-pressure Fe₃O₄ polymorph: experimental and theoretical study. *Journal of Physics: Condensed Matter*, 15, 7697.
- Evrard, O., Malaman, B., Jeannot, F., Courtois, A., Alebouyeh, H., and Gerardin, R. (1980). *Mise*

en évidence de $\text{CaF}^2\text{e}_4\text{O}_6$ et détermination des structures cristallines des ferrites de calcium $\text{CaFe}_{2+n}\text{O}_{4+n}$ ($n=1, 2, 3$): nouvel exemple d'intercroissance. *Journal of Solid State Chemistry*, 35, 112-119.

Guignard, J., and Crichton, W. A. (2014) Synthesis and recovery of bulk Fe_4O_5 from magnetite, Fe_3O_4 . A member of a self-similar series of structures for the lower mantle and transition zone. *Mineralogical Magazine*, 78.2, 361-371.

Haavik, C., Stølen, S., Fjellvåg, H., Hanfland, M., and Häusermann, D. (2000). Equation of state of magnetite and its high-pressure modification: Thermodynamics of the Fe-O system at high pressure. *American Mineralogist*, 85, 514-523.

Hoppe, R. (1979). Effective coordination numbers (ECoN) and mean fictive ionic radii (MEFIR). *Zeitschrift für Kristallographie-Crystalline Materials*, 150, 23-52.

Izumi, F., and Momma, K. (2007) Three-dimensional visualization in powder diffraction. *Solid State Phenomena*, 130, 15-20.

Jacob, D. E., Piazzolo, S., Schreiber, A., and Trimby, P. (2016). Redox-freezing and nucleation of diamond via magnetite formation in the Earth's mantle. *Nature communications*, 7, 11891.

Larson, A.C. and Von Dreele, R.B. (2000) General structure analysis system (GSAS). Los Alamos National Laboratory Report, LAUR, 86-748.

Lavina, B., Dera, P., Kim, E., Meng, Y., Downs, R.T., Weck, P.F., Sutton, S.R., and Zhao, Y.

(2011) Discovery of the recoverable high-pressure iron oxide Fe_4O_5 . Proceedings of the National Academy of Science, 108, 17281-17285.

Lavina, B., and Meng, Y. (2015) Unraveling the complexity of iron oxides at high pressure and

temperature: Synthesis of Fe_5O_6 . Science Advances 1, no.5, e1400260.

Malaman, B., Alebouyeh, H., Jeannot, F., Courtois, A., Gerardin, R., and Evrard, O. (1981).

Préparation et caractérisation des ferrites de calcium $\text{CaFe}_{2+n}\text{O}_{4+n}$ A valeurs fractionnaires de n (3/2, 5/2) et leur incidence sur le diagramme Fe-Ca-O A 1120°C. Materials Research Bulletin, 16, 1139-1148.

Momma, K. and Izumi, F. (2011) VESTA 3 for three-dimensional visualization of crystal,

volumetric and morphology data. Journal of applied crystallography, 44, 1272-1276.

Myhill, B., Ojwang, D.O., Ziberna, L., Frost, D., Boffa Ballaran, T., and Miyamjima, N. (2016).

On the P-T-fO₂ stability of Fe_4O_5 and Fe_5O_6 -rich phases: a thermodynamic and experimental study. Contributions to Mineralogy and Petrology, 171, 1-11.

Schollenbruch, K., Woodland, A.B., Frost, D.J., Wang, Y., Sanehira, T., and Langenhorst, F.

(2011) In situ determination of the spinel-post-spinel transition in Fe_3O_4 at high pressure and temperature by synchrotron X-ray diffraction. American Mineralogist, 96, 820-827.

- Shannon, R.D. (1976) Revised effective ionic radii and systematic studies of interatomic distances in halides and chalcogenides. *Acta Crystallographica*, A32, 751-767.
- Sinmyo, R., Bykova, E., Ovsyannikov, S.V., McCammon, C., Kuppenko, I., Ismailova, L., and Dubrovinsky, L. (2016) Discovery of Fe₇O₉: a new iron oxide with a complex monoclinic structure. *Nature scientific reports*, 6, 32852.
- Temple, P. A. and Hathaway, C. E. (1973). Multiphonon Raman spectrum of silicon. *Physical Review B*, 7, 3685.
- Toby, B.H. (2001) EXPGUI, a graphical user interface for GSAS. *Journal of Applied Crystallography*, 34, 210-213.
- Toraya, H. (1990). Array-type universal profile function for powder pattern fitting. *Journal of applied crystallography*, 23, 485-491.
- Uenver-Thiele, L., Woodland, A.B., Boffa Ballaran, T., Miyajima, N., and Frost, D.J. (2017a) Phase relations of MgFe₂O₄ at conditions of the deep upper mantle and transition zone. *American Mineralogist*, 102, 632–642.
- Uenver-Thiele L, Woodland AB, Boffa Ballaran T, Miyajima N, Frost DJ (2017b) Phase relations of Fe-Mg spinels including new high-pressure post-spinel phases and implications for natural samples. *American Mineralogist*, 102, 2054-2064.

Uenver-Thiele, L., Woodland, A. B., Miyajima, N., Ballaran, T. B., and Frost, D. J. (2018).

Behavior of Fe_4O_5 – $\text{Mg}_2\text{Fe}_2\text{O}_5$ solid solutions and their relation to coexisting Mg–Fe silicates and oxide phases. *Contributions to Mineralogy and Petrology*, 173, 1-16.

Walker, D., Carpenter, M. A., and Hitch, C. M. (1990). Some simplifications to multianvil devices for high pressure experiments. *American Mineralogist*, 75, 1020-1028.

Woodland, A.B., Frost, D.J., Trots, D.M., Klimm, K., Mezouar, M. (2012) In situ observation of the breakdown of magnetite (Fe_3O_4) to Fe_4O_5 and hematite at high pressures and temperatures. *American Mineralogist*, 97, 1808-1811.

Woodland, A.B., Uenver-Thiele, L., and Boffa Ballaran, T. (2015) Synthesis of Fe_5O_6 and the high-pressure stability of Fe^{2+} - Fe^{3+} -oxides related to Fe_4O_5 . *Goldschmidt Abstracts 2015*, 3446.

Woodland, A.B., Uenver-Thiele, L., and Boffa Ballaran, T. (2016) High P-T stability of Fe_5O_6 and its coexistence with other Fe-oxides. 2nd European Mineralogical Conference (emc2016) Rimini, Italy, S14-4 (abs).

FIGURE CAPTIONS

Figure 1. Rietveld refinement of $\text{Mg}_{0.87}\text{Fe}_{8.13}\text{O}_{11}$. The XRD pattern was collected at ambient

pressure and temperature. Data points (brown) and solid lines (green) represent the observed and the calculated profiles, respectively, and the residual is shown at the bottom. The background profiles are solid lines (black). Tick marks indicate the Bragg peak positions. The upper and lower ticks are for $\text{Ca}_2\text{Fe}_7\text{O}_{11}$ -type $\text{Mg}_{0.87}\text{Fe}_{8.13}\text{O}_{11}$ and silicon, respectively. The inset illustrates the high 2θ region with an expanded intensity scale.

Figure 2. Crystal structure of $\text{Ca}_2\text{Fe}_7\text{O}_{11}$ -type $\text{Mg}_{0.87}\text{Fe}_{8.13}\text{O}_{11}$. The unit-cell is shown with solid lines. The small spheres are oxygen.

Figure 3. Structural relationships among high-pressure Mg-Fe oxides as a function of $\text{Fe}^{3+}/(\text{Mg}+\Sigma\text{Fe})$ ratio. (a) Fe_5O_6 - $\text{Mg}_3\text{Fe}_2\text{O}_6$ (Lavina et al. 2015; Uenver-Thiele et al. in preparation) (b) Fe_9O_{11} - $\text{MgFe}_8\text{O}_{11}$ (Woodland et al. 2016; this study) (c) Fe_4O_5 - $\text{Mg}_2\text{Fe}_2\text{O}_5$ (Lavina et al. 2011; Boffa Ballaran et al. 2015) (d) Fe_7O_9 - $\text{Mg}_3\text{Fe}_4\text{O}_9$ (Sinmyo et al. 2016; Uenver-Thiele et al. 2017) (e) CT-type Fe_3O_4 (Haavik et al. 2000). Non-equivalent sites are indicated by different colors. Black dashed boxes are edge-shared octahedral chains. Green dashed boxes represent incorporated chains from structures with higher Fe^{3+} content in the sequence of smaller two-way arrows. Larger two-way arrows indicate incorporation or removal of two single octahedral chains. Smaller two-way arrows represent incorporation or removal of one of the single octahedral chain. Unit-cells are represented using solid-line boxes.

Table 1. Interatomic distances and angles in the structures of Mg_{0.9}Fe_{8.1}O₁₁.

Bond distance (Å)			Bond angle (°)		
<u>M1 site</u>					
M1-O3×2	2.319(14)	Average	2.206	O3-M1-O3	77.1(6)
M1-O4×2	2.118(15)	BVS	1.71	O4-M1-O4	86.1(8)
M1-O5×2	2.180(12)	<i>n_c</i>	5.66	O5-M1-O5	83.1(6)
		Poly. V. (Å ³)	10.24	M4-O4-M5	122.7(11)
<u>M2 site</u>					
M2-O5×2	2.053(17)	Average	1.992	O6-M2-O6	94.9(8)
M2-O6×4	1.962(13)	BVS	2.98	O6-M2-O6	85.1(8)
		<i>n_c</i>	5.90	O5-M2-O5	180
		Poly. V. (Å ³)	10.49		
<u>M3 site</u>					
M3-O1×2	2.064(4)	Average	2.097	O2-M3-O1	93.2(3)
M3-O2×2	2.158(10)	BVS	2.19	O1-M3-O1	88.9(2)
M3-O2	2.144(14)	<i>n_c</i>	5.77	O2-M3-O2	84.1(5)
M3-O3	1.996(16)	Poly. V. (Å ³)	12.20	O2-M3-O3	172.0(7)
<u>M4 site</u>					
M4-O1	2.442(5)	Average (VI)	2.055	O3-M4-O2	85.5(6)
M4-O2×2	2.013(10)	Average (V) ^a	1.977	O3-M4-O3	91.9(6)
M4-O3×2	1.986(15)	BVS	2.95	O2-M4-O2	83.2(5)
M4-O4	1.890(16)	<i>n_c</i>	5.00	O1-M4-O4	176.0(7)
		Poly. V. (Å ³) ^a	5.79		
<u>M5 site</u>					
M5-O4	1.898(17)	Average (VI)	2.127	O5-M5-O5	86.8(8)
M5-O5×2	2.104(15)	Average (V) ^a	2.089	O6-M5-O6	83.6(7)
M5-O6×2	2.170(14)	BVS	2.36	O5-M5-O6	00392.7(5)
M5-O6	2.314(18)	<i>n_c</i>	4.75	O6-M5-O4	176.8(8)
		Poly. V. (Å ³) ^a	6.51		

BVS = bond valence sum (Brown and Altermatt, 1985) and *n_c* = effective coordination number (Hoppe, 1979) were calculated considering 6 cation-oxygen distances. Poly. V. = polyhedral

volume.

^aCalculated considering a 5-fold coordination excluding the longest bond.

Figure 1

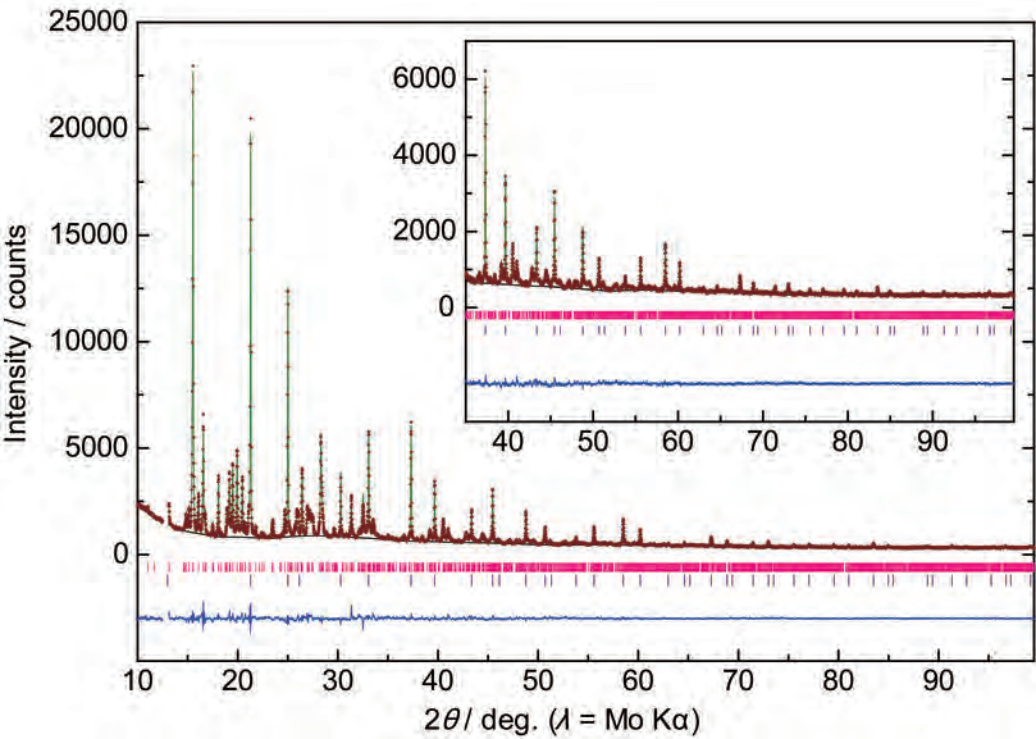
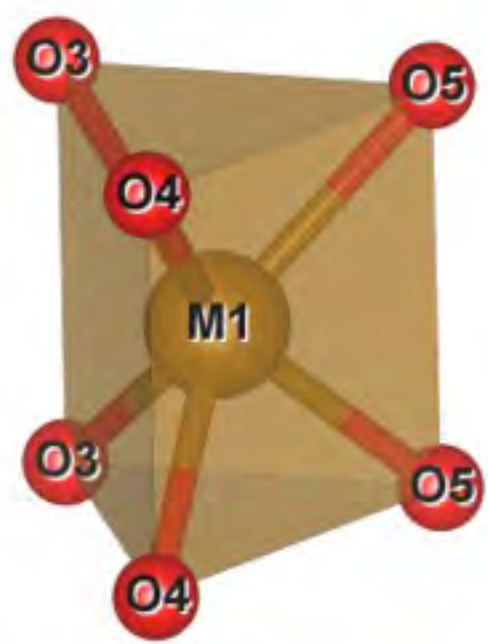
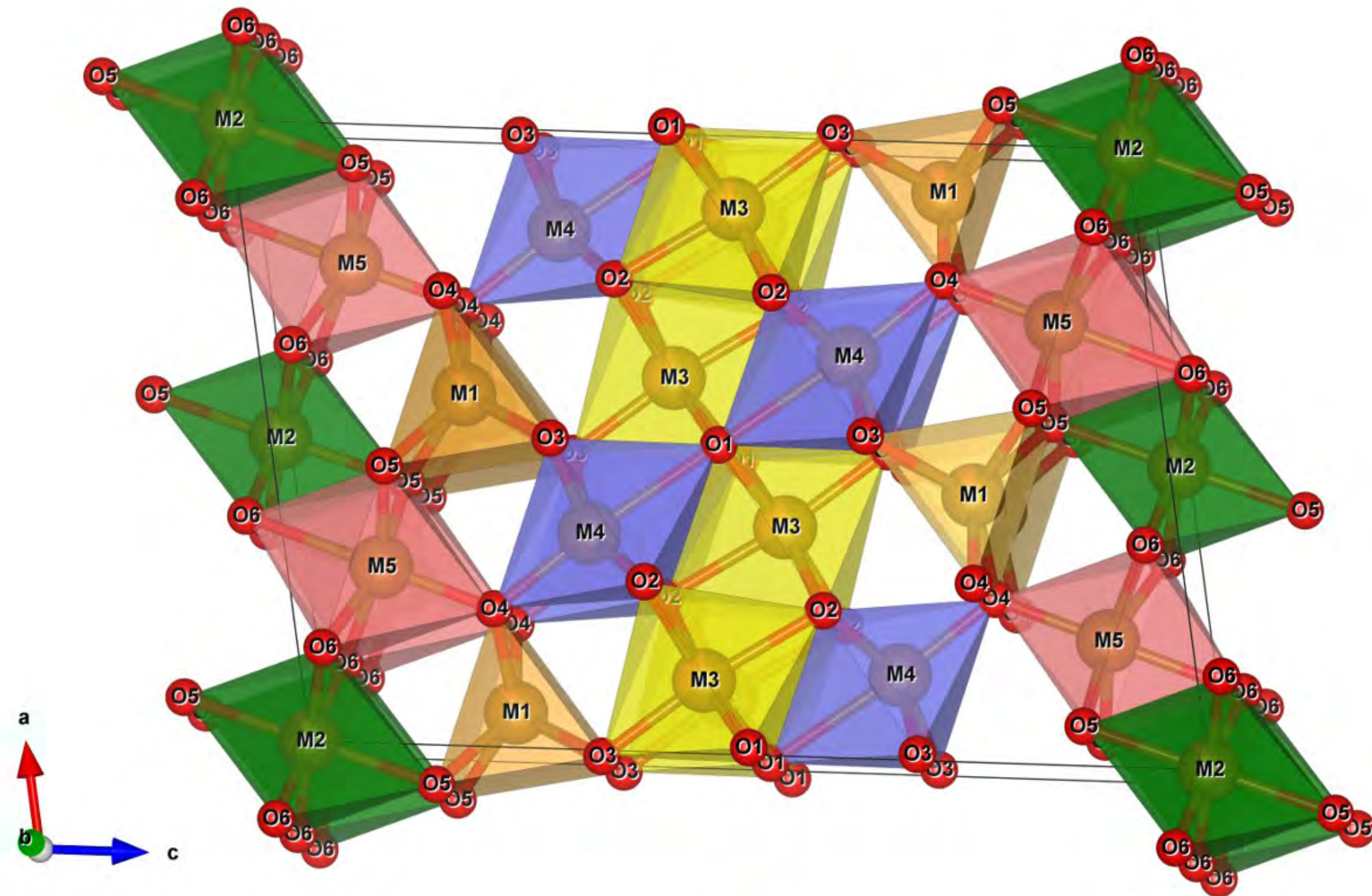
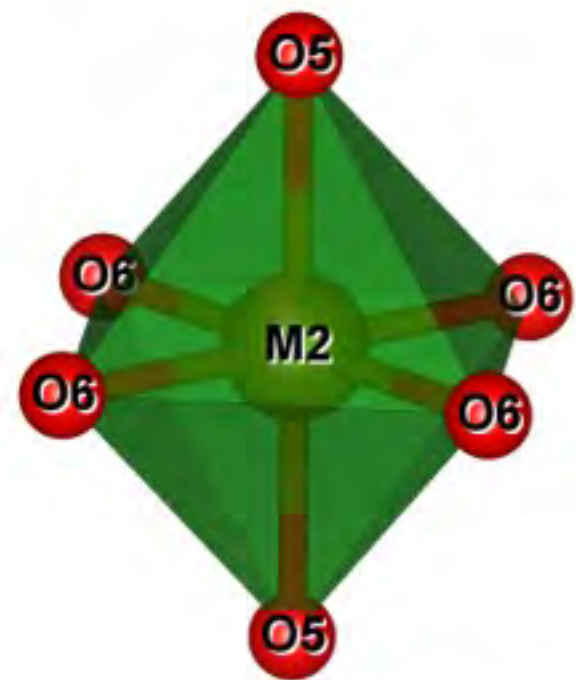


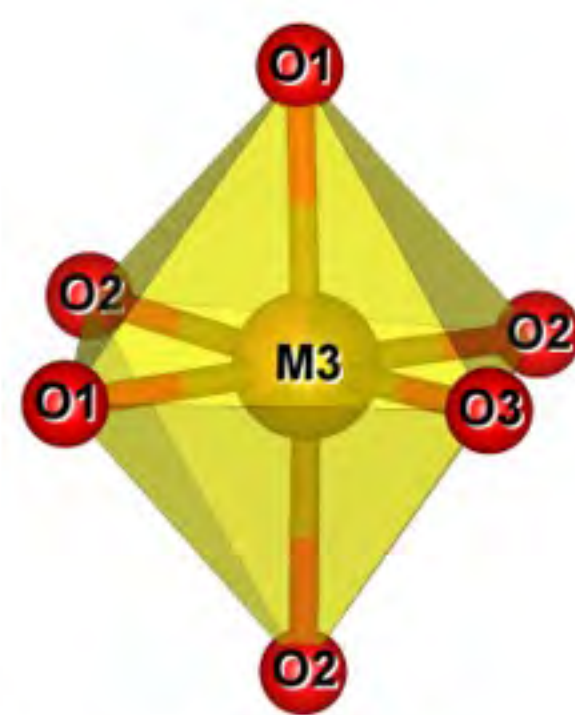
Figure 2



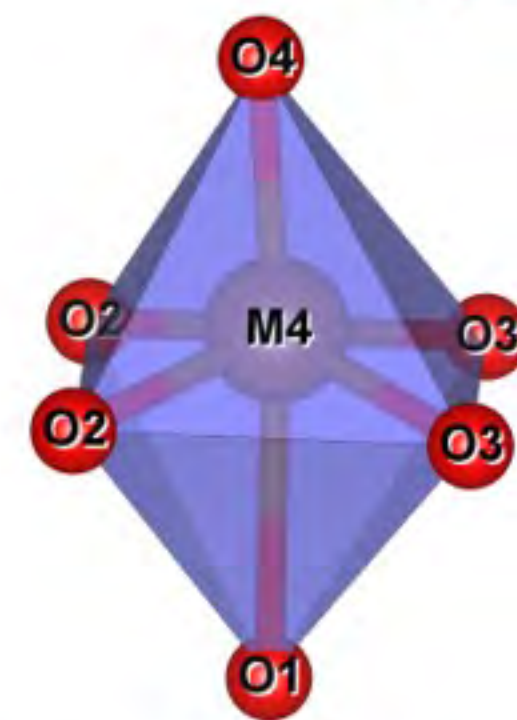
M1O₆ trigonal prism



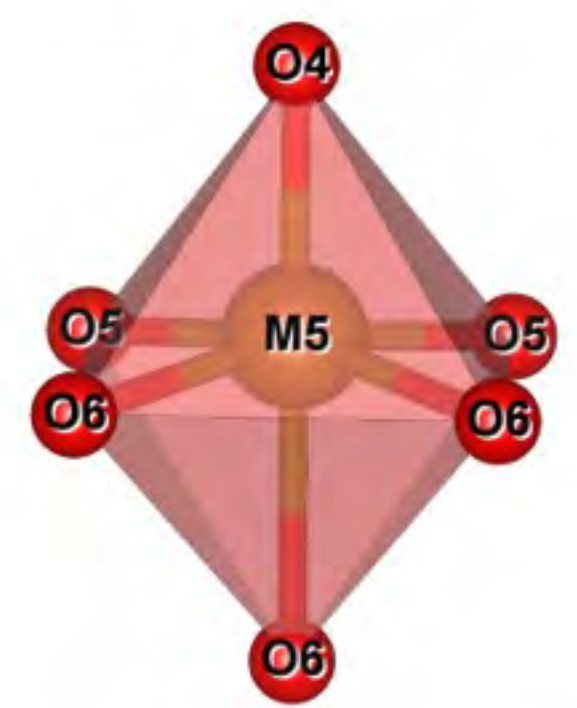
M2O₆ octahedron



M3O₆ octahedron



M4O₆ octahedron



M5O₆ octahedron

Figure 3

